

# Building 3D Morphable Models from a Single Scan

Skylar Sutherland

Massachusetts Institute of Technology  
77 Massachusetts Ave, Cambridge, MA 02139  
skylar@mit.edu

Bernhard Egger

egger@mit.edu

Joshua Tenenbaum

jbt@mit.edu

## Abstract

*We propose a method for constructing generative models of 3D objects from a single 3D mesh. Our method produces a 3D morphable model that represents shape and albedo in terms of Gaussian processes. We define the shape deformations in physical (3D) space and the albedo deformations as a combination of physical-space and color-space deformations. Whereas previous approaches have typically built 3D morphable models from multiple high-quality 3D scans through principal component analysis, we build 3D morphable models from a single scan or template. As we demonstrate in the face domain, these models can be used to infer 3D reconstructions from 2D data (inverse graphics) or 3D data (registration). Specifically, we show that our approach can be used to perform face recognition using only a single 3D scan (one scan total, not one per person), and further demonstrate how multiple scans can be incorporated to improve performance without requiring dense correspondence. Our approach enables the synthesis of 3D morphable models for 3D object categories where dense correspondence between multiple scans is unavailable. We demonstrate this by constructing additional 3D morphable models for fish and birds and use them to perform simple inverse rendering tasks. We share the code used to generate these models and to perform our inverse rendering and registration experiments.*

## 1. Introduction

3D generative models of objects are used in many computer vision and graphics applications. Present methods for constructing such models typically require either significant amounts of 3D data processed through specialized pipelines, substantial manual annotation, or extremely large amounts of 2D data [10, 12]. We explore a novel approach that could provide a means to build generative models from very limited data: a single 3D object scan. The models we build are 3D morphable models (3DMMs) [3, 12], a type of genera-

tive model which creates samples by applying randomized shape and albedo deformations to a reference mesh. Traditionally, 3DMMs (e.g. [28, 13, 19, 5]) are built through principal component analysis (PCA) applied to datasets of 50 to 10,000 3D meshes produced by specialized (and expensive) 3D scanners [12]. Furthermore, a registration step is required to align the scans to a common topology. In contrast, we use only a single scan or template, and so can eschew registration, an intrinsically ill-posed problem. While our method’s performance depends on the choice of template, PCA-based 3DMMs face the same issue since registration likewise requires a choice of common topology.

Our approach uses the provided scan as our generative model’s mean and smoothly deforms the scan as a surface in physical (3D) space and color (RGB) space using Gaussian processes. Our shape deformation model follows that of [20]. We define the albedo deformations by combining analogous smooth albedo deformations on the mesh with smooth deformations on the surface defined by considering the mesh as a shape in RGB-space, with each vertex’s location determined by its albedo rather than its position. We initially define very generic Gaussian processes and add domain-specificity through correlation between color channels and bilateral symmetry. Our models are fully compatible with PCA-based 3DMMs; the only difference is that our models’ covariances are constructed through Gaussian processes rather than PCA. As our 3DMMs use the same format and support the same operations as PCA-based 3DMMs, they can be used in existing pipelines to perform downstream tasks. They can additionally be used to augment PCA-based 3DMMs [21].

This is, to the best of our knowledge, the most data-efficient procedure currently extant for constructing 3D generative models, and the sole procedure that only uses a single datapoint. While the performance of our models is significantly poorer than that of PCA-based 3DMMs, they nevertheless perform surprisingly well given their data-efficiency. While 3DMMs are a common prior in computer vision systems, their scalability is limited because their synthesis involves careful capture and modeling with category-

specific domain knowledge. Our method’s data-efficiency obviates the need for large amounts of data capture, while our method’s generality enables its use for any object class. Finally, our approach minimizes the amount of sensitive personal data required to construct face 3DMMs.

We also prototype an extension of our single-scan approach to a multi-scan setting by constructing mixture models of separate single-scan 3DMMs. This can be seen as a generalization of kernel density estimation (KDE). While performing inference with such a mixture model is more computationally expensive than with a PCA-based 3DMM, we demonstrate that the reconstruction quality obtained is much higher if the number of scans used in the models is low. Furthermore, constructing this type of KDE-based model does not require correspondence between scans.

Although we demonstrate the applicability of our approach to other object categories, we focus our experiments on faces. This is mainly because 3DMMs have historically been built for face modeling, so we can better compare our models to prior work in a face setting, and do so through well-established pipelines. Our results with other object categories are harder to interpret, since our method is unique not only in its ability to generalize from a single datapoint, but also in its flexibility of object category.

The main contributions of this work are the following:

1. We offer a novel albedo deformation model by combining surface-based and color-space-based kernels.
2. We introduce a framework for 3DMM construction from a single 3D scan by extending an existing framework to build statistical shape models [20] with our albedo deformation model.
3. We evaluate our model on three downstream tasks: inverse rendering (2D to 3D registration), face recognition, and 3D to 3D registration. We compare its performance with that of the 2019 Basel Face Model [13], a state-of-the-art 3DMM produced from 200 3D scans.
4. We build a prototype KDE-based face model from 10 face scans, and demonstrate that on a face recognition task it outperforms a PCA-based 3DMM built from the same 10 scans.

The source code used in this paper is available at <https://github.com/skyler-sutherland/single-scan-3dmm>.

## 1.1. Related Work

The idea of building an axiomatic shape deformation model using Gaussian processes was previously explored in [20], which used such a deformation model as a prior for 3D registration tasks. We extend this approach to include albedo along with shape by building Gaussian processes in RGB-space as well as physical space. This enables its use as prior in an inverse graphics setting, and allows us to take albedo into account during registration. [17] presented a method for 3D reconstruction of faces from 2D images through axiomatic deformation of a single 3D scan. However, unlike our approach, this paper did not produce a

generative model, and performed 3D reconstruction through shape-from-shading rather than probabilistic inference, using the 3D scan as purely as regularizer. [39] applied a Gaussian process intensity model in medical imaging for co-registration of CT and MRI images and for data augmentation. Other shape representation strategies (e.g. [18]) incorporate geodesic distances instead of Euclidean distances; while geodesic distances are beneficial in modeling motion and expression, since they are not easily transferable to color spaces we here focus on Euclidean distance. [27] proposes a method for modeling variability in 3D datasets without correspondence by deforming a single template mesh. However, unlike our work, [27] learns a nonlinear deformation model from a significant number of (unregistered) 3D scans through dimensionality reduction techniques, and so is inapplicable given only a single scan. Furthermore, they only study 3D-to-3D reconstruction and it is unclear how their approach could be applied in a computer vision setting.

While classically 3DMMs have been built from a collection of 3D scans, there are also several approaches that start from 2D data or combine 2D and 3D data. Building a 3DMM solely from 2D data was first explored by [9]. Although they, like us, also start from a 3D mean shape as an initial template, their work neglects albedo. Recently, methods to improve 3DMMs through 2D observations were proposed [41, 43]. While they seek to build 3DMMs from 2D data, their approaches start with a full 3DMM built from 3D scans, and primarily refine the appearance model to increase flexibility. Neither method offers a way to derive this initial model other than capturing 3D data and establishing correspondence between scans. [42] further extended these ideas to incorporate nonlinear models so as to overcome the limitations inherent in the linearity of classical 3DMMs. In contrast to these works aiming to build a 3DMM from a large collection of 2D data and an initial 3DMM, our work focuses on building a 3DMM from just a single 3D scan. Such a model could be used as an initial model for the 2D learning strategies discussed above.

Additionally, some recent work has focused on the problem of the unsupervised learning of 3D generative models from a large 2D training corpus [38, 46] or from depth data [1]. The 3D generative models learned by these approaches do not disentangle illumination and albedo (or neglect albedo entirely, as in [1]), and do not preserve correspondence, making them difficult to interpret. Furthermore, this means that they are incompatible with existing 3DMM-based pipelines; in contrast, generative models produced through our approach can be used interchangeably with PCA-based 3DMMs. [40] was the first to propose a complete 3DMM learned from 2D images and video data through self-supervised learning, using an average 3D face for initialization. This paper is more directly comparable to our work; however, we show that the average face is already

sufficient to produce a usable 3DMM, without any 2D data.

Other works have focused on extending 3D morphable models beyond a linear latent space [29, 6, 42]. In contrast, we use a traditional linear latent space and rather focus on how such latent spaces can be learned. For additional work on applications of 3DMMs and shape and albedo representations used with 3DMMs, we refer to [12].

In addition to 3D morphable models, our work can also be connected with *shape-from-template* approaches to 3D vision. These approaches typically address the following problem: given a reference mesh, an input image, and a set of dense (pixel-level) correspondences between the input image and a rendering of the mesh [2, 50, 7, 22, 25, 31] or with the mesh directly [26, 32], deform the mesh to match the input image. Restrictions on the allowed deformations (e.g. isometry or conformality) make this problem well-posed and sometimes solvable analytically. This framing means that shape-from-template approaches are rarely applicable without dense 2D correspondence annotations and generally ignore albedo. Shape-from-template approaches that do not require dense 2D correspondence have typically previously relied on additional 3D or video data and still do not fully model albedo [47, 33, 36]. In contrast, our approach can infer 3D reconstructions from single images using only a small set of landmarks (sparse 2D correspondence) for localization. We furthermore separate albedo and illumination and fully incorporate albedo in our deformations.

## 2. Methods

A 3DMM consists of a shape model and an albedo model; samples from a 3DMM are meshes with a common topology, with the positions and albedo of each vertex generated by the 3DMM’s shape and albedo models, respectively [12]. Our framework represents samples from the shape and albedo models as deformations of a vertex-colored mesh that defines both the topology of all samples and the mean of the shape and albedo distributions. Our approach uses the 3D scan as the mean of the resulting 3DMM. We define the shape and albedo models in terms of Gaussian processes, each consisting of a mean and a covariance kernel [20, 30].

We define a Gaussian process  $g$  as a pair  $(\mu, \Sigma)$ , where  $\mu$  is the mean of the Gaussian process and  $\Sigma$  is the covariance kernel of the Gaussian process;  $\mu$  is a function from  $A$  to  $\mathbb{R}^n$  for some set  $A$  and constant  $n$ , and  $\Sigma$  is a positive-definite function from  $A^2$  to  $\mathbb{R}^{n \times n}$ , where  $\mathbb{R}^{n \times n}$  is the space of  $n$ -by- $n$  matrices. In our case, for both the shape and albedo models,  $A$  is the set of mesh vertices, and  $n = 3$ . A sample from the shape model maps  $A$  to positions in  $\mathbb{R}^3$ , whereas a sample from the albedo model maps  $A$  to RGB values, represented as vectors in  $\mathbb{R}^3$ . We represent our shape and albedo kernels using Mercer decomposition computed through the Nyström method [30, 20].

### 2.1. Shape Covariance Kernels

We follow the approach of [20]: defining covariance kernels which give a high correlation between nearby points and a low correlation between distant points. The most straightforward way to do this is with physical distance. Our shape kernels are based on radial basis function kernels [30, 20].

A function  $f : A^2 \rightarrow \mathbb{R}$  is positive-definite if the matrix  $M$  defined by  $M_{i,j} = f(x_i, x_j)$  is positive-semidefinite for any  $x_1, \dots, x_n \in \mathbb{R}$  [23]. This definition can be extended to matrix-valued kernels by letting  $M_{i,j}$  represent a block submatrix of  $M$  instead of an entry of  $M$  [30, 20]. Since the set of positive-semidefinite matrices is closed under addition and positive scalar multiplication [15], so are matrix-valued kernels. In order to create a kernel with a coarse-to-fine structure, possessing strong short-range correlations and weaker long-range correlations, we define our shape kernel as a linear combination of radial basis function kernels. Letting  $\Sigma_{s,\sigma}$  represent the radial basis function kernel defined using physical distance as its metric and scale  $\sigma$ , we define the family of scalar kernels  $\Sigma_{\text{std}}(a, b, c, A, B, C) = a\Sigma_{s,A} + b\Sigma_{s,B} + c\Sigma_{s,C}$ . We here let  $\Sigma_0 = \Sigma_{\text{std}}(a_s, b_s, c_s, A_s, B_s, C_s)$ , where  $a_s, b_s, c_s, A_s, B_s$ , and  $C_s$  are hyperparameters (listed in Section 2.4).

In order to represent 3D deformations, we must multiply scalar kernels by 3-by-3 matrices. Since we do not wish for there to be correlations between deformations in  $x, y$ , and  $z$ , we simply multiply by  $I_3$ , the 3-by-3 identity matrix. Thus, our standard shape kernel is  $K_s = I_3 \Sigma_0$ . One limitation of this kernel is that it does not encode bilateral symmetry. Many object categories, including faces, are bilaterally symmetric. In order to add symmetry to this kernel, we wish to make the deformations applied to points on opposite sides of the object closely correlated in the up-down and forward-back axes and strongly anticorrelated in the left-right axis [24]. To define such kernels, let  $\Phi_m \in \mathbb{R}^{3 \times 3}$  be the matrix which, considered as a linear transformation applied to points in physical space, negates a point’s left-right component (where left and right are defined relative to the scan). Then our symmetric shape kernel is defined as  $K_s^{\text{sym}} = I_3 \Sigma_0(x, y) + \alpha \Phi_m \Sigma_0(x, \Phi_m(y))$ , where  $\Phi_m(y)$  denotes applying  $\Phi_m$  as a linear transformation to  $y$ ’s position in  $\mathbb{R}^3$ , and  $\alpha$  is a hyperparameter (listed in Section 2.4).

### 2.2. Albedo Covariance Kernels

What we principally desire in an albedo kernel is that deformations applied to different areas should be highly correlated if and only if the areas are related. Unlike shape deformations, albedo deformations in general need not be spatially continuous, and so a global notion of similarity is needed in addition to physical proximity. We measure the similarity of mesh vertices by combining their distance in physical space with their distance in albedo space.

Physical distance is a straightforward way of assessing

similarity. We define a physical distance-based albedo kernel similarly to  $K_s$ . Specifically, we define  $K_{a,xyz} = I_3 \Sigma_{xyz}$ , where  $\Sigma_{xyz} = \Sigma_{\text{std}}(a_a, b_a, c_a, A_a, B_a, C_a)$ , with hyperparameters  $a_a, b_a, c_a, A_a, B_a$ , and  $C_a$  listed in Section 2.4. Samples from  $K_{a,xyz}$  represent deformations in RGB-space, not position. However, this kernel neglects some kinds of similarity. For instance, in a human face, a point on a lip is more similar to another point on a lip than it is to an equidistant point on a cheek; more generally, many objects exhibit part-based similarity in addition to distance-based similarity. Color-space distance provides us with an estimate of part-based similarity that does not depend on explicit part annotations. Just as the distances between mesh points in physical space (in the mean) constitute a metric on the set of mesh points, so do the Euclidean distances between mesh points' albedos, represented as RGB values and considered as points in  $\mathbb{R}^3$ . Using this alternate metric, we may define another family of radial basis function kernels, which we term  $\Sigma_{a,\sigma}$  for  $\sigma \in \mathbb{R}$ . We then define the alternate albedo kernel  $K_{a,rgb} = I_3 \Sigma_{rgb}$ , where  $\Sigma_{rgb} = d \Sigma_{a,D}$ , with hyperparameters  $d$  and  $D$  (listed in Section 2.4).

To use both local and global information, we average these kernels. Our primary contribution is the combined kernel  $K_a = 0.5(K_{a,xyz} + K_{a,rgb})$ . This kernel takes into account both the difference in position and difference in albedos between points on the mesh, and can thus relatively robustly assess whether different parts of the object are parts of the same component.

As stated, all three of our albedo kernels are products of a scalar-valued kernel with  $I_3$ . Multiplying by a different matrix enables us to incorporate domain knowledge about an object category's common albedos by correlating the different color channels (red, green, and blue). In particular, as a very rough approximation to human skin tones, we introduce additional kernels  $K_{a,xyz}^{\text{cor}}$  and  $K_{a,rgb}^{\text{sym}}$ , depending, respectively, on physical and RGB-space distance. Letting

$$M_x = \begin{bmatrix} 1 & x & x \\ x & 1 & x \\ x & x & 1 \end{bmatrix} \quad (1)$$

we define  $K_{a,xyz}^{\text{cor}} = M_\beta \Sigma_{xyz}$  and  $K_{a,rgb}^{\text{sym}} = M_\gamma \Sigma_{rgb}$ , where  $\beta$  and  $\gamma$  are hyperparameters (listed in Section 2.4).

To add further domain knowledge we create additional albedo kernels that incorporate bilateral symmetry. Since the albedo of a member of a bilaterally symmetric object class is essentially bilaterally symmetric,  $K_{a,rgb}^{\text{sym}}$  is already symmetric in practice. However, the physical-distance-based albedo kernels can be symmetrized via a process analogous to that used for the shape kernels, with the difference that we do not wish to negate left-right deformations located on opposite sides of the object. We choose to consider color channel correlations and symmetry simultaneously, and so define  $K_{a,xyz}^{\text{sym}}(x, y) = K_{a,xyz}^{\text{cor}}(x, y) + \alpha K_{a,xyz}^{\text{cor}}(x, \Phi_m y)$ ,

and define  $K_a^{\text{sym}} = 0.5(K_{a,rgb}^{\text{sym}} + K_{a,xyz}^{\text{sym}})$ .

To attempt to separate the roles played by symmetry and color-channel correlation, in the supplementary material we also present results with albedo kernels that have correlated color channels but lack symmetry.

### 2.3. Kernel Density Estimation

One limitation of our approach is that it provides no way to leverage the information present in multiple scans. However, an extension of our approach can be used in a setting where multiple scans are available. To construct a model from multiple scans, we create single-scan 3DMMs for each scan separately, and then build a mixture model from the different 3DMMs built from each individual scan, resulting in a non-parametric 3DMM-based model. This essentially amounts to an extension of kernel density estimation (KDE), where Gaussian processes replace uniform Gaussian distributions in the definitions of each mixture component, providing a non-uniform noise model.

An advantage of this kernel density estimation approach is that, unlike PCA, it does not require dense correspondence between scans. This could enable the creation of 3DMM-based generative models of object categories where many 3D scans exist but where establishing dense correspondence is impossible (e.g. chairs). However, the non-parametric nature of a KDE-based model means that, unlike a PCA-based 3DMM, the amount of computation required to perform inference grows with the number of scans.

### 2.4. Choices of Hyperparameters

We choose as hyperparameters  $a_s = 7, b_s = 5, c_s = 3, A_s = 100, B_s = 50, C_s = 10, a_a = 0.02, b_a = 0.01, c_a = 0.01, A_a = 500, B_a = 20, C_a = 2, d = 0.015, D = 0.15, \alpha = 0.7, \beta = 0.9375$ , and  $\gamma = 0.95$ . Importantly, these parameters have generally not been extensively tuned, which is reflected in the fact that we use the same kernels for faces, birds and fish. Our core idea is simply to combine radial basis function kernels at three different scales and magnitudes so as to incorporate global as well as local flexibility. Hyperparameters representing physical distances (namely  $a_s, b_s, c_s, A_s, B_s, C_s, A_a, B_a$ , and  $C_a$ ) have units of millimeters. We represent RGB values as points in  $[0, 1]^3$ , and  $a_a, b_a, c_a, d$ , and  $D$  represent distances or magnitudes in color space using this unit system.

## 3. Experiments

We produce a set of 3DMMs from our kernels using the average face of the 2019 Basel Face Model [13] as our reference mesh. These are listed with their corresponding kernels in Table 1. These 3DMMs have the same mean as the 2019 Basel Face Model, and so comparing their performance with that of the 2019 Basel Face Model constitutes a direct comparison of our axiomatic Gaussian process-based covariance



name	shape kernel	albedo kernel
standard-full	$K_s$	$K_a$
standard-RGB	$K_s$	$K_{a,rgb}$
standard-XYZ	$K_s$	$K_{a,xyz}$
symmetric-full	$K_s^{sym}$	$K_a^{sym}$
symmetric-RGB	$K_s^{sym}$	$K_{a,rgb}^{sym}$
symmetric-XYZ	$K_s^{sym}$	$K_{a,xyz}^{sym}$

Table 1: Our Gaussian processes for modeling faces.

kernels with the learned covariance model of the 2019 Basel Face Model. We also produce 3DMMs by combining our kernels with face scans provided with the 2009 Basel Face Model [28]. We assess these models’ performance on downstream tasks where 3DMMs are often used, namely inverse graphics and registration. In Section 3.3 we experiment with simple 3DMMs of birds and fish.

Samples from our shape and albedo kernels applied to the mean of the 2019 Basel Face Model [13] (i.e. our core 3DMMs) are provided in the supplementary material. The supplementary material also includes an evaluation of the specificity, generalization, and compactness [37] of our face 3DMMs relative to the Basel Face Model. Those results suggest both that our 3DMMs can adequately capture the distribution of human faces, and that the choice of template only weakly affects their performance. However, it is important to note that we do *not* claim that our face 3DMMs accurately capture the distribution of human faces, or that samples from them are naturalistic; rather, we claim that our 3DMMs perform well on various computer vision tasks.

### 3.1. Inverse Rendering

One of the most direct ways to assess the value of our model is to apply it in an analysis-by-synthesis setting [48]. Using our 3DMMs as priors on 3D meshes, we can perform inverse rendering to reconstruct 3D meshes from 2D images through approximate posterior inference [35]. We use a spherical harmonics lighting model, as in [49], and a pinhole camera model, as in [3]. Since no synthetic image will ever exactly match a natural image, we treat foreground pixels as subject to Gaussian noise and background pixels as sampled from the input image, following the method of [34].

To perform inference, we use the Markov chain Monte Carlo (MCMC) method presented in [35]. Specifically, we use Gaussian drift proposals to update pose, perform closed-form estimation of illumination, and use Gaussian drift proposals applied in the 3DMM’s low-dimensional eigenspaces to update the mesh itself. In order to locate the face in the image we constrain pose using landmark annotations provided with each image. Although we generated these landmark annotations manually, they could also have been obtained automatically using existing tools (e.g. OpenPose [8]).

One analysis-by-synthesis task is to reconstruct 3D face meshes from natural images, render the results and compare them with said natural images. We here perform this task on images from the Labeled Faces in the Wild dataset [16] and show in Figure 1 the reconstructions produced using the standard-full and symmetric-full 3DMMs (as defined in Table 1), as well as the reconstructions that our inverse graphics pipeline produces using the 2019 Basel Face Model [13]. As Figure 1 demonstrates, all of these 3DMMs produce high-quality reconstructions.

In addition to the models we define using the mean of the 2019 Basel Face Model, we construct additional 3DMMs using the symmetric kernel and ten scans provided with the 2009 Basel Face Model [28] as different means. We name these models symmetric- $x$ , where  $x$  is the ID number of the scan (001, 002, 006, 014, 017, 022, 052, 053, 293, or 323). Reconstructions produced by these 3DMMs can be found in the supplementary material, along with side views of our reconstructions. To assess our 3DMMs’ performance in an inverse graphics setting where the choice of prior gains importance, the supplementary material also includes reconstructions of partially occluded faces produced with the occlusion-aware MCMC method described in [11]. All models again yield similar reconstruction quality.

**Face recognition:** In our second experiment, we use the inverse rendering approach of Section 3.1.1 to perform face recognition, as outlined in [35, 13, 4]. By reconstructing the shape and albedo latents from a gallery of reference images  $\{f_1, \dots, f_n\}$  (with one image per identity), we can obtain latents  $(c_{s,i}, c_{a,i})$  for each reference image  $f_i$ . Faces in a novel image  $f_0$  are then identified by reconstructing shape and albedo latents  $(c_{s,0}, c_{a,0})$  from said image and determining the reference image with the maximum cosine angle in the joint shape-albedo latent space, as in [4]. We conduct face recognition on images from the CMU Multi-PIE database [14]. The results are presented in Table 2.

Table 2 illustrates that the 3DMMs with albedo kernels that combine RGB-space and physical-space distance information perform face recognition significantly more accurately on all image types than do 3DMMs with albedo kernels that only make use of one type of distance metric. Furthermore, we may observe that the performance of the symmetric model is better on all image types than that of the BU3D-FE model [13], a 3DMM built from 100 3D scans. Table 2 also illustrates that 3DMMs defined using the mean of the 2019 Basel Face Model have better performance than those defined using individual face scans. This is particularly true on images with a yaw angle over  $15^\circ$ , since as the yaw angle increases, the prior (in this case the 3DMM) plays a larger role in generating the reconstruction.

**Inference with kernel density estimation:** The previously presented face recognition results relied on the mean of the 2019 Basel Face Model [13]. The performance of the



Figure 1: Reconstructions produced from natural images using various 3DMMs. The first row shows the natural images used as input, while the remaining rows show the reconstructions inferred using different 3DMMs. The standard-full and symmetric-full models were produced using the mean of the 2019 Basel Face Model [13] as template.

3DMMs built using individual face scans (symmetric-001 to symmetric-323) is also listed in Table 2. The performance of these 3DMMs is clearly significantly lower than that of the symmetric-full 3DMM. However, by combining the information present in the 10 scans through our KDE approach, we can produce a new model that achieves performance comparable to that of the symmetric-full 3DMM. To perform face recognition with this non-parametric model, we perform inference for each mixture component separately on both the probe image and each gallery image. We then compute the cosine-angle in latent space between the probe reconstruction and all gallery reconstructions for each mixture component, and classify the probe image based on which 3DMM and gallery image yields the smallest cosine-angle.

The performance of this mixture model on our face recognition task is listed in Table 2 as “10-scan KDE”. As Table 2 shows, this approach offers face recognition performance comparable to that achieved by the symmetric-full 3DMM, and outperforms the BU3D-FE model on all yaw levels, despite using only 10 scans. To provide a more direct comparison between our novel KDE approach and PCA-based 3DMMs, we also produced a 3DMM by performing PCA with the 10 scans. The face recognition performance of this 3DMM is listed in Table 2 as “10-scan PCA”. Table 2 demonstrates that this PCA-based 3DMM has far poorer face recognition performance than our KDE-based model. In fact, the performance of the 10-scan PCA-based 3DMM is comparable to that of the 3DMMs produced from a single individual face scan (symmetric-001 to symmetric-323).

### 3.2. Registration Tasks

Registration is another task for which 3DMMs are used. In this task we wish to transform an arbitrary face mesh into a mesh with a given topology while preserving the face as closely as possible. Prior work has nearly exclusively relied

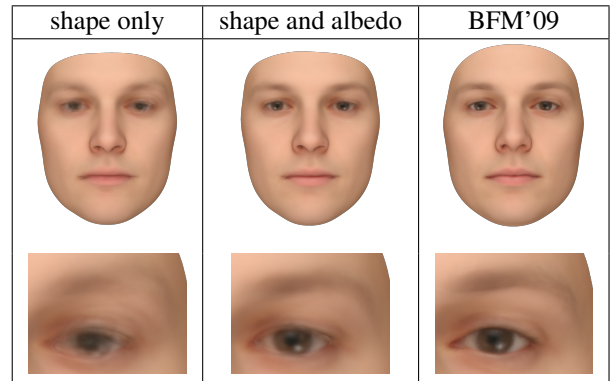


Figure 2: The average of the registration results produced by the MCMC methods using both shape and albedo information (“shape and albedo”) or shape information only (“shape only”) on all ten scans, along with the average of the corresponding registered meshes produced in the construction (strongly reliant on manual landmark annotations) of the 2009 Basel Face Model [28] (“BFM’09”). Close-ups of the left eye and eyebrow are provided, illustrating that the eyebrows and the pupils of the eyes are far less clearly defined in the shape-only condition.

on shape information to compute such a transformation [12]. However, albedo information also provides important constraints on face registration. For instance, the eyebrows and the pupils of the eyes are almost entirely defined by albedo.

To perform registration tasks with our 3DMMs, we adapted the inverse rendering approach of [35] to minimize the chamfer distance between the model mesh and the target mesh while simultaneously minimizing the pixel error between the rendered model instance and the rendered target mesh. We achieve this by combining an image-based

angle	15°	30°	45°
probe id	140_16	130_16	080_16
standard-full	84.7	69.9	54.2
standard-RGB	76.3	57.8	28.9
standard-XYZ	77.1	62.7	35.7
symmetric-full	<b>93.2</b>	<b>85.9</b>	<b>72.3</b>
symmetric-RGB	73.5	61.4	40.2
symmetric-XYZ	73.1	58.6	44.2
symmetric-001	78.7	62.2	49.8
symmetric-002	78.7	70.7	48.6
symmetric-006	77.5	63.9	38.2
symmetric-014	71.9	59.0	47.8
symmetric-017	<b>88.0</b>	72.3	50.6
symmetric-022	85.9	73.5	59.4
symmetric-052	85.9	71.5	55.0
symmetric-053	84.3	<b>76.7</b>	55.4
symmetric-293	85.5	74.3	<b>59.8</b>
symmetric-323	87.6	76.3	55.4
10-scan PCA	86.0	65.9	42.2
10-scan KDE	<b>94.0</b>	<b>85.9</b>	<b>71.5</b>
BU3D-FE [13]	90.4	82.7	68.7
BFM '17 [13]	<b>98.8</b>	<b>98.0</b>	<b>90.0</b>

Table 2: Face recognition results for images from the Multi-PIE database [14]. Each column represents the accuracy for a set of probe images with a common yaw angle given in the first row. The second row gives the common ending of the IDs in the Multi-PIE dataset of the probe images with a given yaw angle. The gallery is constructed from the images of all 249 identities with a yaw angle of 0° (dataset IDs ending in 051\_16). Chance rate is 0.4. The 3DMMs in the second box (standard-full to symmetric-XYZ) were produced using the mean of the 2019 Basel Face Model [13], while the 3DMMs in the third box (symmetric-001 to symmetric-323) were produced using the 3D scans provided with the 2009 Basel Face Model [28]. BFM '17 refers to the 2017 Basel Face Model [13].

reconstruction likelihood, which constrains 2D appearance, with a shape-based likelihood, which enforces 3D shape consistency as measured by chamfer distance. This minimizes shape distance and induces albedo consistency while establishing correspondence with the topology of our 3DMM's template. While both those ideas are often applied in isolation, they are rarely combined in registration tasks (or only combined as post-processing). We roughly align the meshes to initialize the pose, but, unlike typical approaches, do not use landmarks during registration. Instead, the location of facial features is constrained by the albedo component of the evaluation. As post-processing we eliminate any net translation using the method of [44] and set each vertex's albedo by projecting vertex normals onto the scan as in [13].

This process enables us to make use of both shape and albedo information in registration. We compare the result of doing so with the analogous registration result produced using only shape information in our MCMC process. We apply both registration methods to the unprocessed meshes for face scans 001, 002, 006, 014, 017, 022, 052, 053, 293, and 323. To do so we use the standard-full 3DMM with the mean of the highest point-count version of the 2019 Basel Face Model [13] as reference. To evaluate our registration we build a 3DMM from the registration results using principal component analysis.

We compare these results with the registration used by the 2009 Basel Face Model [28], which used shape information along with manual landmark annotations. Figure 2 demonstrates that by using shape and albedo information our registration process produces a sharp and stable albedo reconstruction whose quality is comparable to that of the 2009 Basel Face Model's registration, and far superior to that produced using shape information alone. This performance is impressive, since the 2009 Basel Face Model heavily relied on human-provided landmark annotations in its registration pipeline, whereas our approach requires no annotations.

The supplementary material contains a quantitative assessment of our shape registration performance, and shows that including albedo information in registration slightly increases the shape error. This is unsurprising, as the shape-only reconstruction is optimized to produce the lowest shape error possible, and the shape and albedo reconstruction by definition cannot have less than the minimum shape error. However, as Figure 2 demonstrates, the shape and albedo reconstruction has far higher quality overall.

### 3.3. Constructing 3DMMs for Other Objects

We have thus far focused on 3DMM for faces; we now demonstrate that analogous methods can be used to build 3DMMs for other object categories. Specifically, we construct single-scan 3DMMs for fish and birds using as references synthetic meshes with simple manual coloring.<sup>1</sup> These meshes are simple artistic models and were constructed without 3D scanning. We can build 3DMMs from each of these references using the same kernels as used in standard-full and symmetric-full, i.e.  $K_s$  and  $K_a$  in the first case, and  $K_s^{\text{sym}}$  and  $K_a^{\text{sym}}$  in the second. This produces two new 3DMMs for each mesh, which we term the standard and symmetric models for each object category. As our reference meshes lack many details that 3D scans possess, the performance of these 3DMMs is likely much lower than that of single-scan 3DMMs built from 3D scans. Results with additional fish and bird 3DMMs produced with the  $K_{a,xyz}$  and  $K_{a,xyz}^{\text{sym}}$

<sup>1</sup>Our bird and fish reference meshes are obtained from, respectively, <https://www.blendswap.com/blend/11752> and <https://www.turbosquid.com/3d-models/free-tail-animation-3d-model/368484>



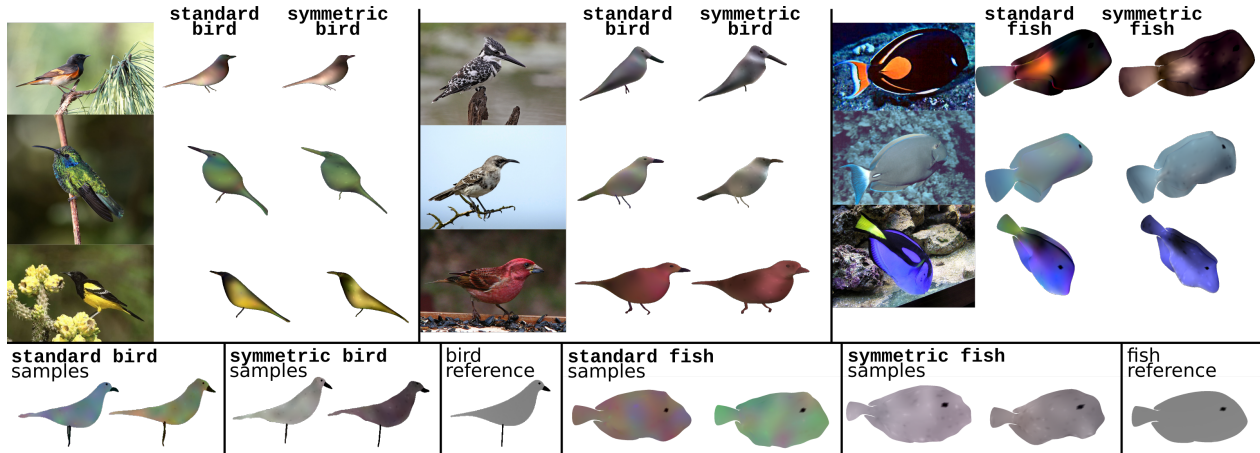


Figure 3: On the upper left and middle: the reconstructions produced by the standard and symmetric bird models on six images taken from the Caltech-UCSD Birds 200 dataset [45]. On the upper right: the reconstructions produced by the standard and symmetric fish models on three public-domain images taken from Wikipedia. On the bottom: samples from the standard and symmetric bird and fish models, shown in side views, as well as the reference meshes used to build these 3DMMs.

albedo kernels are presented in the supplementary material.

We seek to model a wide range of birds, but restrict ourselves to simple standing poses. We restrict ourselves to the *Acanthurus* genus of fish, which possesses a wide range of color variability but lack the fine details (such as scales) that many other fish possess. In Figure 3, we show qualitative reconstruction results along with samples from our bird and fish models and the reference meshes used to construct them. While these reconstructions are not as accurate as those in Figure 1, they do capture some rough features. We suggest that three main factors make birds a more difficult object category than faces: birds have a much more complex albedo, including high-frequency components that our models capture poorly; birds have a well-defined silhouette, whereas faces have somewhat arbitrary boundaries; and color-correlation, while beneficial in modeling faces, impedes the symmetric bird model’s ability to model birds. Our standard model’s performance on fish seems somewhat better, likely due to the lack of high-frequency components. The symmetric model does much more poorly on fish, likely because the correlation of its color channels impedes its ability to model the regional color variation of fish. It is important to keep in mind, however, that our method’s performance is not directly comparable to that of other, less data-efficient approaches.

## 4. Conclusion

Our research demonstrates that applying Gaussian process-based deformations to a single 3D scan can yield a generative model which, though of lower-quality than 3DMMs produced through PCA, can still be used in many

contexts where hand-produced 3DMMs have previously been required. This approach to 3DMM construction is far more data-efficient than prior approaches and eliminates the complex pipelines, often involving manual annotation, required to establish dense correspondence between multiple 3D scans. For object categories where the number of available scans is extremely limited or where dense correspondence between scans cannot be easily obtained, this procedure thus offers a promising method for building 3DMMs. Additionally, our results demonstrate the high value of fully integrating albedo into the 3DMM pipeline, and show that this can be done by combining covariance kernels which produce spatially continuous deformations with kernels that produce color-space-continuous deformations. In addition to the results demonstrated in this paper, we believe our method can be highly beneficial in addressing dataset bias, which is a limitation of all currently available 3DMMs. In particular, models built with our KDE approach, and PCA-based 3DMMs augmented with our single-scan models, may generalize better than traditional PCA-based 3DMMs.

## Acknowledgement

This work was funded by the DARPA Learning with Less Labels (LwLL) program (Contract No: FA8750-19-C-1001), the DARPA Machine Common Sense (MCS) program (Award ID: 030523-00001) and by the Center for Brains, Minds and Machines (CBMM) (NSF STC award CCF-1231216). B.Egger is supported by a PostDoc Mobility Grant, Swiss National Science Foundation P400P2\_191110.



## References

- [1] V. F. Abrevaya, S. Wuhrer, and E. Boyer. Multilinear autoencoder for 3D face model learning. In *2018 IEEE Winter Conference on Applications of Computer Vision (WACV)*, pages 1–9, Mar. 2018. [2](#)
- [2] A. Bartoli, Y. Gérard, F. Chadebecq, and T. Collins. On template-based reconstruction from a single view: Analytical solutions and proofs of well-posedness for developable, isometric and conformal surfaces. In *2012 IEEE Conference on Computer Vision and Pattern Recognition*, pages 2026–2033, June 2012. ISSN: 1063-6919. [3](#)
- [3] Volker Blanz and Thomas Vetter. A morphable model for the synthesis of 3D faces. In *Proceedings of the 26th annual conference on Computer graphics and interactive techniques*, pages 187–194, 1999. [1](#), [5](#)
- [4] V. Blanz and T. Vetter. Face recognition based on fitting a 3D morphable model. *IEEE Transactions on Pattern Analysis and Machine Intelligence*, 25(9):1063–1074, Sept. 2003. Conference Name: IEEE Transactions on Pattern Analysis and Machine Intelligence. [5](#)
- [5] James Booth, Anastasios Roussos, Allan Ponniah, David Dunaway, and Stefanos Zafeiriou. Large scale 3D morphable models. *International Journal of Computer Vision*, 126(2):233–254, 2018. [1](#)
- [6] Giorgos Bouritsas, Sergiy Bokhnyak, Stylianos Ploumpis, M. Bronstein, and S. Zafeiriou. Neural 3D morphable models: Spiral convolutional networks for 3D shape representation learning and generation. *2019 IEEE/CVF International Conference on Computer Vision (ICCV)*, 2019. [3](#)
- [7] Florent Brunet, Richard Hartley, Adrien Bartoli, Nassir Navab, and Remy Malgouyres. Monocular template-based reconstruction of smooth and inextensible surfaces. In Ron Kimmel, Reinhard Klette, and Akihiro Sugimoto, editors, *Computer Vision – ACCV 2010*, Lecture Notes in Computer Science, pages 52–66, Berlin, Heidelberg, 2011. Springer. [3](#)
- [8] Zhe Cao, Gines Hidalgo, Tomas Simon, Shih-En Wei, and Yaser Sheikh. OpenPose: Realtime multi-person 2D pose estimation using part affinity fields. *arXiv:1812.08008 [cs]*, May 2019. arXiv: 1812.08008. [5](#)
- [9] Thomas J Cashman and Andrew W Fitzgibbon. What shape are dolphins? Building 3D morphable models from 2D images. *IEEE transactions on pattern analysis and machine intelligence*, 35(1):232–244, 2012. [2](#)
- [10] Siddhartha Chaudhuri, Daniel Ritchie, Jiajun Wu, Kai Xu, and Hao Zhang. Learning generative models of 3D structures. In *Computer Graphics Forum*, volume 39, pages 643–666. Wiley Online Library, 2020. [1](#)
- [11] Bernhard Egger, Sandro Schönborn, Andreas Schneider, Adam Kortylewski, Andreas Morel-Forster, Clemens Blumer, and Thomas Vetter. Occlusion-aware 3d morphable models and an illumination prior for face image analysis. *International Journal of Computer Vision*, 126(12):1269–1287, 2018. [5](#), [14](#), [20](#)
- [12] Bernhard Egger, William AP Smith, Ayush Tewari, Stefanie Wuhrer, Michael Zollhoefer, Thabo Beeler, Florian Bernard, Timo Bolkart, Adam Kortylewski, Sami Romdhani, et al. 3D morphable face models—past, present, and future. *ACM Transactions on Graphics (TOG)*, 39(5):1–38, 2020. [1](#), [3](#), [6](#)
- [13] Thomas Gerig, Andreas Morel-Forster, Clemens Blumer, Bernhard Egger, Marcel Lüthi, Sandro Schönborn, and Thomas Vetter. Morphable face models—an open framework. In *2018 13th IEEE International Conference on Automatic Face & Gesture Recognition (FG 2018)*, pages 75–82. IEEE, 2018. [1](#), [2](#), [4](#), [5](#), [6](#), [7](#), [12](#), [13](#), [14](#), [16](#), [17](#), [20](#)
- [14] Ralph Gross, Iain Matthews, Jeffrey Cohn, Takeo Kanade, and Simon Baker. Multi-PIE. *Image and Vision Computing*, 28(5):807–813, May 2010. [5](#), [7](#), [12](#)
- [15] Roger A. Horn. *Matrix Analysis: Second Edition*. Cambridge University Press, New York, NY, 2 edition edition, Oct. 2012. [3](#)
- [16] Gary B Huang, Marwan Mattar, Tamara Berg, and Eric Learned-Miller. Labeled faces in the wild: A database for studying face recognition in unconstrained environments. 2008. [5](#), [14](#), [17](#), [19](#), [20](#)
- [17] Ira Kemelmacher-Shlizerman and Ronen Basri. 3D face reconstruction from a single image using a single reference face shape. *IEEE transactions on pattern analysis and machine intelligence*, 33(2):394–405, 2010. [2](#)
- [18] Martin Kilian, Niloy J Mitra, and Helmut Pottmann. Geometric modeling in shape space. In *ACM SIGGRAPH 2007 papers*, pages 64–es. 2007. [2](#)
- [19] Tianye Li, Timo Bolkart, Michael J. Black, Hao Li, and Javier Romero. Learning a model of facial shape and expression from 4D scans. *ACM Transactions on Graphics*, 36(6):194:1–194:17, Nov. 2017. [1](#)
- [20] Marcel Lüthi, Thomas Gerig, Christoph Jud, and Thomas Vetter. Gaussian process morphable models. *IEEE transactions on pattern analysis and machine intelligence*, 40(8):1860–1873, 2017. [1](#), [2](#), [3](#)
- [21] Marcel Lüthi, Andreas Forster, Thomas Gerig, and Thomas Vetter. Shape modeling using Gaussian process morphable models. In Guoyan Zheng, Shuo Li, and Gabor Székely, editors, *Statistical Shape and Deformation Analysis*, pages 165–191. Academic Press, Jan. 2017. [1](#)
- [22] A. Malti, A. Bartoli, and T. Collins. A pixel-based approach to template-based monocular 3D reconstruction of deformable surfaces. In *2011 IEEE International Conference on Computer Vision Workshops (ICCV Workshops)*, pages 1650–1657, Nov. 2011. [3](#)
- [23] J. Mercer. Functions of positive and negative type, and their connection with the theory of integral equations. *Philosophical Transactions of the Royal Society of London. Series A, Containing Papers of a Mathematical or Physical Character*, 209:415–446, 1909. [3](#)
- [24] Andreas Morel-Forster. *Generative shape and image analysis by combining Gaussian processes and MCMC sampling*. PhD thesis, University of Basel, 2016. [3](#)
- [25] Francesc Moreno-Noguer, Josep M. Porta, and Pascal Fua. Exploring ambiguities for monocular non-rigid shape estimation. In Kostas Daniilidis, Petros Maragos, and Nikos Paragios, editors, *Computer Vision – ECCV 2010*, Lecture Notes in Computer Science, pages 370–383, Berlin, Heidelberg, 2010. Springer. [3](#)

- [26] F. Moreno-Noguer, M. Salzmann, V. Lepetit, and P. Fua. Capturing 3D stretchable surfaces from single images in closed form. In *2009 IEEE Conference on Computer Vision and Pattern Recognition*, pages 1842–1849, June 2009. ISSN: 1063-6919. 3
- [27] Maks Ovsjanikov, Wilnot Li, Leonidas Guibas, and Niloy J. Mitra. Exploration of continuous variability in collections of 3D shapes. *ACM Transactions on Graphics*, 30(4):33:1–33:10, July 2011. 2
- [28] Pascal Paysan, Reinhard Knothe, Brian Amberg, Sami Romdhani, and Thomas Vetter. A 3D face model for pose and illumination invariant face recognition. In *2009 Sixth IEEE International Conference on Advanced Video and Signal Based Surveillance*, pages 296–301. IEEE, 2009. 1, 5, 6, 7, 14, 16, 19
- [29] Anurag Ranjan, Timo Bolkart, Soubhik Sanyal, and Michael J. Black. Generating 3D faces using convolutional mesh autoencoders. In Vittorio Ferrari, Martial Hebert, Cristian Sminchisescu, and Yair Weiss, editors, *Computer Vision – ECCV 2018*, Lecture Notes in Computer Science, pages 725–741, Cham, 2018. Springer International Publishing. 3
- [30] Carl Edward Rasmussen. Gaussian processes in machine learning. In *Summer School on Machine Learning*. Springer, 2003. 3
- [31] M. Salzmann and P. Fua. Linear local models for monocular reconstruction of deformable surfaces. *IEEE Transactions on Pattern Analysis and Machine Intelligence*, 33(5):931–944, May 2011. Conference Name: IEEE Transactions on Pattern Analysis and Machine Intelligence. 3
- [32] Mathieu Salzmann, Francesc Moreno-Noguer, Vincent Lepetit, and Pascal Fua. Closed-form solution to non-rigid 3D surface registration. In David Forsyth, Philip Torr, and Andrew Zisserman, editors, *Computer Vision – ECCV 2008*, Lecture Notes in Computer Science, pages 581–594, Berlin, Heidelberg, 2008. Springer. 3
- [33] M. Salzmann, R. Urtasun, and P. Fua. Local deformation models for monocular 3D shape recovery. In *2008 IEEE Conference on Computer Vision and Pattern Recognition*, pages 1–8, June 2008. ISSN: 1063-6919. 3
- [34] Sandro Schönborn, Bernhard Egger, Andreas Forster, and Thomas Vetter. Background modeling for generative image models. *Computer Vision and Image Understanding*, 136:117–127, 2015. 5
- [35] Sandro Schönborn, Bernhard Egger, Andreas Morel-Forster, and Thomas Vetter. Markov chain Monte Carlo for automated face image analysis. *International Journal of Computer Vision*, 123(2):160–183, 2017. 5, 6
- [36] A. Shaji, A. Varol, L. Torresani, and P. Fua. Simultaneous point matching and 3D deformable surface reconstruction. In *2010 IEEE Computer Society Conference on Computer Vision and Pattern Recognition*, pages 1221–1228, June 2010. ISSN: 1063-6919. 3
- [37] Martin A Styner, Kumar T Rajamani, Lutz-Peter Nolte, Gabriel Zsemlye, Gábor Székely, Christopher J Taylor, and Rhodri H Davies. Evaluation of 3d correspondence methods for model building. In *Biennial International Conference on Information Processing in Medical Imaging*, pages 63–75. Springer, 2003. 5, 14, 16
- [38] Attila Szabó, Givi Meishvili, and Paolo Favaro. Unsupervised generative 3d shape learning from natural images. *arXiv preprint arXiv:1910.00287*, 2019. 2
- [39] Nicolas H Nbonsou Tegang, Jean-Rassaire Fouefack, Bhushan Borotikar, Valérie Burdin, Tania S Douglas, and Tinashe EM Mutsvangwa. A gaussian process model based generative framework for data augmentation of multi-modal 3d image volumes. In *International Workshop on Simulation and Synthesis in Medical Imaging*, pages 90–100. Springer, 2020. 2
- [40] Ayush Tewari, Hans-Peter Seidel, Mohamed Elgharib, Christian Theobalt, et al. Learning complete 3d morphable face models from images and videos. *arXiv preprint arXiv:2010.01679*, 2020. 2
- [41] Ayush Tewari, Michael Zollhöfer, Pablo Garrido, Florian Bernard, Hyeonwoo Kim, Patrick Pérez, and Christian Theobalt. Self-supervised multi-level face model learning for monocular reconstruction at over 250 Hz. In *Proceedings of the IEEE Conference on Computer Vision and Pattern Recognition*, pages 2549–2559, 2018. 2
- [42] Luan Tran, Feng Liu, and Xiaoming Liu. Towards high-fidelity nonlinear 3D face morphable model. In *Proceedings of the IEEE Conference on Computer Vision and Pattern Recognition*, pages 1126–1135, 2019. 2, 3
- [43] Luan Tran and Xiaoming Liu. On learning 3D face morphable model from in-the-wild images. *IEEE transactions on pattern analysis and machine intelligence*, 2019. 2
- [44] S. Umeyama. Least-squares estimation of transformation parameters between two point patterns. *IEEE Transactions on Pattern Analysis and Machine Intelligence*, 13(4):376–380, Apr. 1991. Conference Name: IEEE Transactions on Pattern Analysis and Machine Intelligence. 7
- [45] Catherine Wah, Steve Branson, Peter Welinder, Pietro Perona, and Serge J. Belongie. The Caltech-UCSD Birds-200-2011 dataset. 2011. 8, 13
- [46] Shangzhe Wu, Christian Rupprecht, and Andrea Vedaldi. Unsupervised learning of probably symmetric deformable 3d objects from images in the wild. In *Proceedings of the IEEE/CVF Conference on Computer Vision and Pattern Recognition*, pages 1–10, 2020. 2
- [47] R. Yu, C. Russell, N. D. F. Campbell, and L. Agapito. Direct, dense, and deformable: Template-based non-rigid 3D reconstruction from RGB video. In *2015 IEEE International Conference on Computer Vision (ICCV)*, pages 918–926, Dec. 2015. ISSN: 2380-7504. 3
- [48] Alan Yuille and Daniel Kersten. Vision as Bayesian inference: analysis by synthesis? *Trends in cognitive sciences*, 10(7):301–308, 2006. 5
- [49] Jasenko Zivanov, Andreas Forster, Sandro Schönborn, and Thomas Vetter. Human face shape analysis under spherical harmonics illumination considering self occlusion. In *2013 International Conference on Biometrics (ICB)*, pages 1–8, June 2013. ISSN: 2376-4201. 5
- [50] Jonas Östlund, Aydin Varol, Dat Tien Ngo, and Pascal Fua. Laplacian meshes for monocular 3D shape recovery. In Andrew Fitzgibbon, Svetlana Lazebnik, Pietro Perona, Yoichi Sato, and Cordelia Schmid, editors, *Computer Vision – ECCV*

2012, Lecture Notes in Computer Science, pages 412–425,  
Berlin, Heidelberg, 2012. Springer. 3

# Appendices

## A. Color-Correlated Asymmetric 3DMMs

In our main paper we build 3DMMs using Gaussian processes that include symmetry and color-channel correlation heuristics. To assess the effects of these heuristics individually, we can also build 3DMMs that include only one of these heuristics. Specifically, we experimented with constructing 3DMMs whose albedo models have correlated color channels but which lack symmetry. This enables us to compare the relative importance in an analysis-by-synthesis setting of the symmetry and color-correlation heuristics of our symmetric 3DMMs.

Our main paper defined albedo kernels  $K_{a,xyz}^{\text{cor}}$  and  $K_{a,rgb}^{\text{sym}}$ . These kernels possess a color-channel correlation heuristic but lack an explicit symmetry heuristic ( $K_{a,rgb}^{\text{sym}}$  is symmetric, but this is only because we assume that the reference face is symmetric). We may average these kernels to produce an albedo kernel  $K_a^{\text{cor}} = 0.5(K_{a,rgb}^{\text{sym}} + K_{a,xyz}^{\text{cor}})$  which combines physical-space and RGB-space distance information. Samples from  $K_{a,xyz}^{\text{cor}}$  and  $K_a^{\text{cor}}$  are shown in Figure 4. By combining these albedo kernels with our shape kernel  $K_s$ , we can construct 3DMMs which possess a color-channel correlation heuristic but which lack an explicit symmetry heuristic. We list these 3DMMs in Table 3.

We repeat the face recognition experiment presented in Section 3.1.2 of our main paper with these 3DMMs (once again using the mean of the 2019 Basel Face Model [13] as our reference mesh). The results of this experiment are shown in Table 4, along with a copy of the results with the standard and symmetric 3DMMs that were shown in the main paper. Table 4 demonstrates that the color-correlated asymmetric 3DMMs perform comparably to the symmetric (and color-correlated) 3DMMs on faces with  $15^\circ$  and  $30^\circ$  yaw angles. On faces with  $45^\circ$  yaw angles, they are significantly worse, indicating that (unsurprisingly) a symmetry prior becomes more important as the yaw angle increases. Nevertheless, in general the color-correlated asymmetric 3DMMs perform quite well. This indicates that in an inverse graphics context the color-channel correlation heuristic is more important to our symmetric 3DMMs than the symmetry heuristic is, at least for input images with a low yaw angle.

## B. Samples from Kernels

In Figure 4, we show samples from our various shape and albedo kernels, applied to the mean of the 2019 Basel Face Model [13]. While these samples are clearly non-naturalistic, this does not invalidate the results of Section 3 of our main paper. **We make no claim that our 3DMMs accurately model the distribution of human faces; rather, we claim**

name	shape kernel	albedo kernel
correlated-full	$K_s$	$K_a^{\text{cor}}$
correlated-RGB	$K_s$	$K_{a,rgb}^{\text{cor}}$
correlated-XYZ	$K_s$	$K_{a,xyz}^{\text{cor}}$

Table 3: Our Gaussian processes for modeling faces with color-correlated but asymmetric kernels.

angle	$15^\circ$	$30^\circ$	$45^\circ$
probe id	140_16	130_16	080_16
standard-full	84.7	69.9	54.2
standard-RGB	76.3	57.8	28.9
standard-XYZ	77.1	62.7	35.7
correlated-full	92.4	<b>87.1</b>	66.7
correlated-RGB	71.5	58.6	37.8
correlated-XYZ	76.7	61.4	45.8
symmetric-full	<b>93.2</b>	85.9	<b>72.3</b>
symmetric-RGB	73.5	61.4	40.2
symmetric-XYZ	73.1	58.6	44.2

Table 4: Face recognition results on images from the Multi-PIE database [14]. Each column represents the accuracy for a set of probe images with a common yaw angle given in the first row. The second row gives the common ending of the IDs in the Multi-PIE dataset of the probe images with a given yaw angle. The gallery is constructed from images with a yaw angle of  $0^\circ$  (dataset IDs ending in 051\_16).

**that they are of sufficient quality to be useful in a machine vision context.**

## C. Additional Bird and Fish Models

In our paper we presented bird and fish 3DMMs created analogously to the standard-full and symmetric-full 3DMMs, i.e. with  $K_s$  and  $K_a$ , and with  $K_s^{\text{sym}}$  and  $K_a^{\text{sym}}$ , respectively. We can also define similar bird and fish 3DMMs using albedo kernels that only rely on physical distance; i.e., using  $K_{a,xyz}$  and  $K_{a,xyz}^{\text{sym}}$  instead of  $K_a$  and  $K_a^{\text{sym}}$ . This produces two new 3DMMs for each reference mesh, which for space reasons are listed as listed as “XYZ standard” and “XYZ symmetric”. Figure 5 shows samples from these two bird 3DMMs, as well as reconstructions produced with these models of the bird images that were used in the main paper. Figure 6 shows analogous samples and reconstructions for the two new physical-distance-based fish 3DMMs. The results are close to those produced in the main paper; this is unsurprising given that the 3D mesh used to build these 3DMMs does not include complex coloration, and instead has near-piecewise-constant albedo.

In both Figure 6 and in the main paper, we obtain our input natural fish images from Wikipedia<sup>2</sup>.

<sup>2</sup>The links are:

































$K_s$	$K_s^{\text{sym}}$	$K_{a,xyz}$	$K_{a,rgb}$	$K_a$	$K_{a,xyz}^{\text{cor}}$	$K_{a,rgb}^{\text{cor}}$	$K_a^{\text{cor}}$	$K_{a,xyz}^{\text{sym}}$	$K_a^{\text{sym}}$
									
									
									

Figure 4: Three random samples from each of the shape and albedo kernels applied to the mean of the 2019 Basel Face Model [13] and rendered under ambient illumination. The first two columns are the two shape kernels, while the remaining eight columns are the albedo kernels.

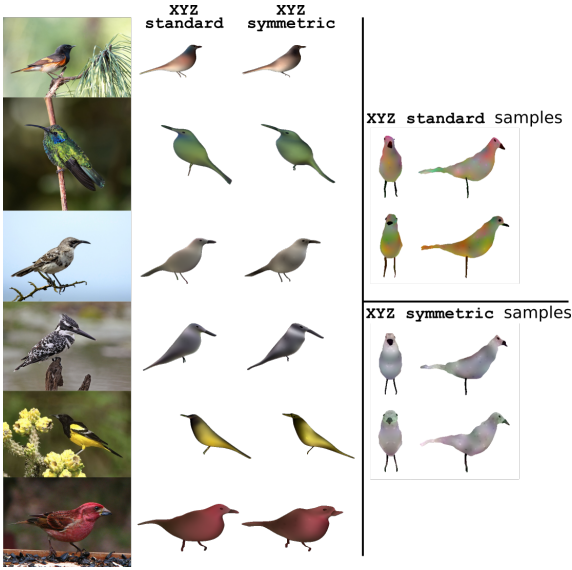


Figure 5: On the left: the reconstructions produced by the two bird models built using only physical distance information on six images taken from the Caltech-UCSD Birds 200 dataset [45]. On the right: samples from these models, shown in frontal and side views.

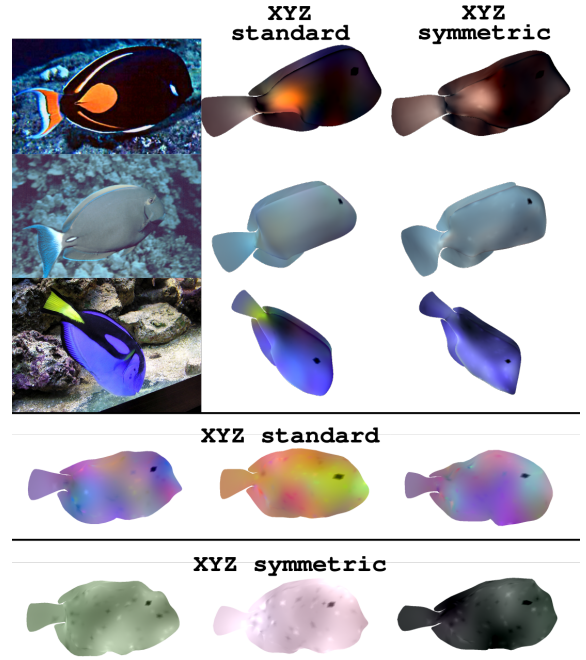


Figure 6: On the top: the reconstructions produced by the two fish models built using only physical distance information on three natural images of fish. On the bottom: samples from these models, shown in side views.

## D. Additional Registration Results

Figures 7, 8, 9, and 10 offer a variety of quantitative metrics of the shape error of the registered meshes produced

[https://en.wikipedia.org/wiki/File:Acanthurus\\_achilles1.jpg](https://en.wikipedia.org/wiki/File:Acanthurus_achilles1.jpg),  
[https://en.wikipedia.org/wiki/File:Acanthurus\\_dussumieri.jpg](https://en.wikipedia.org/wiki/File:Acanthurus_dussumieri.jpg), and  
[https://en.wikipedia.org/wiki/File:Paracanthurus\\_hepatus\\_\(Regal\\_Tang\).jpg](https://en.wikipedia.org/wiki/File:Paracanthurus_hepatus_(Regal_Tang).jpg)

in our paper’s registration tasks. As in the main paper, in all figures the “shape and albedo” option refers to meshes registered using both shape and albedo information in the MCMC method, while the “shape only” option refers to meshes registered using only shape information in the MCMC method. These figures do not take into account the stability of the reconstruction or the albedo error.

We estimate shape error through Hausdorff distance (Figures 7 and 9) and chamfer distance (Figures 8 and 10) between either the vertices of the registered meshes and the corresponding scans (Figures 7 and 8) or a sparse set of landmarks on the registered meshes and corresponding scans (Figures 9 and 10). We obtained landmark information by using the landmark annotations given in [28] for each of the 10 input meshes and the landmark annotations provided with the 2019 Basel Face Model [13] for the registered meshes (since these have the same topology as the 2019 Basel Face Model).

Figures 7 and 8 demonstrate that including albedo information along with shape information slightly increases the shape reconstruction error. As noted in the main text, this is to be expected; the shape-only reconstruction is optimized to produce the lowest shape error possible, whereas the reconstruction produced using both shape and albedo is also optimized to produce a low albedo error, and by definition cannot have a lower shape error than the reconstruction with the minimum shape error. However, the increase in shape error is not very large. Furthermore, Figures 9 and 10 demonstrate that including albedo in registration does not significantly affect the shape error of landmarks. This suggests that the incorporation of albedo information does not reduce the registration quality of the *important aspects* of face shape.

## E. Specificity, Generalization, and Compactness

Figure 11 shows plots of the specificity, generalization, and compactness [37] of our 3DMMs and the 2017 Basel Face Model [13]; specifically, it shows the specificity and generalization of the shape and albedo models of each 3DMM as a function of the number of principal components included. We compare the 2017 Basel Face Model (“BFM 2017”) and versions of the standard-full (“standard”), symmetric-full (“symmetric”), and correlated-full (“correlated”) models built using the mean of the 2017 Basel Face Model as template. We use as our dataset the ten scans provided with the 2009 Basel Face Model [28]. We also include the symmetric- $x$  models, where  $x$  is a scan ID number (001, 002, 006, 014, 017, 022, 052, 053, 293, or 323); for these models we exclude the scan used to build the model. We report results averaged across the symmetric- $x$  models as “single-scan”. We measure specificity and generalization using 1, 2, 5, 10, 20, 50, 100, and all (199) principal compo-

nents. We indicate the specificity and generalization of the mean of the 2017 Basel Face Model, considered as a 3DMM with zero principal components, with a black line.

We may observe that, for all numbers of principal components, the generalization of our 3DMMs’ shape models is comparable to that of the 2017 Basel Face Model, while the generalization of our 3DMMs’ albedo models is in fact superior to that of the 2017 Basel Face Model. The specificity of our 3DMMs’ shape and albedo models, is, of course, inferior to that of the 2017 Basel Face Model. This is unavoidable as our models’ were constructed using far less data than the 2017 Basel Face Model. We may additionally observe that our single-scan models perform comparably to the standard-full model across all conditions.

## F. Qualitative Reconstructions

Figures 12, 13, 14, and 15 provide additional qualitative reconstruction results. Figures 12 and 13 present qualitative reconstructions (in frontal and side views, respectively) of images from the Labeled Faces in the Wild dataset [16] produced using all the 3DMMs constructed using the mean of the 2019 Basel Face Model [13]. Figure 14 presents qualitative reconstructions of the same images produced using 3DMMs built from the scans included with the 2009 Basel Face Model [28]. These reconstructions are significantly lower-quality, because a significant portion of the shape of the template mesh is preserved during the MCMC process. Figure 15 presents qualitative reconstructions of different images from the Labeled Faces in the Wild dataset that contain significant occlusion. Figure 15 includes both 3D reconstructions as well inferred occlusion masks. Figure 15’s results were produced using the occlusion-aware MCMC method described in [11].

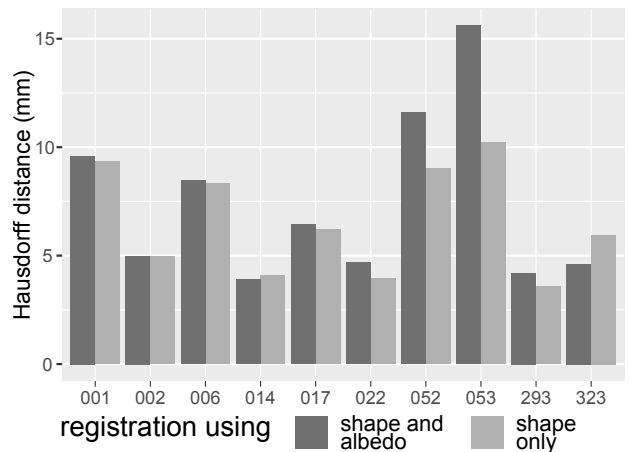


Figure 7: The Hausdorff distance between the vertices of each of the registered meshes and the vertices of the corresponding face scan.

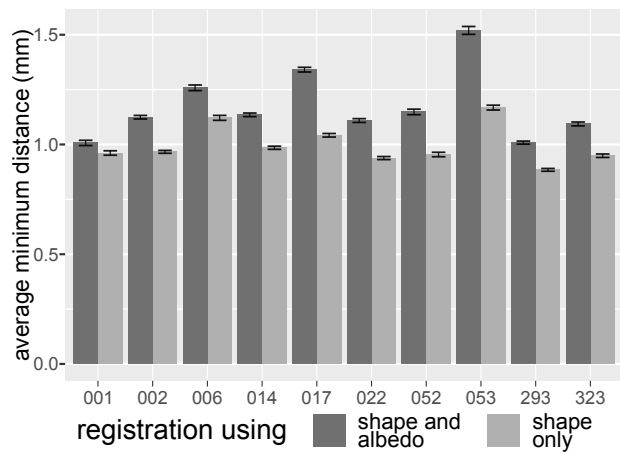


Figure 8: The average distance between each vertex in each of the registered meshes and the closest point in the corresponding face scan, with error bars ( $\pm 1.96$  standard error).

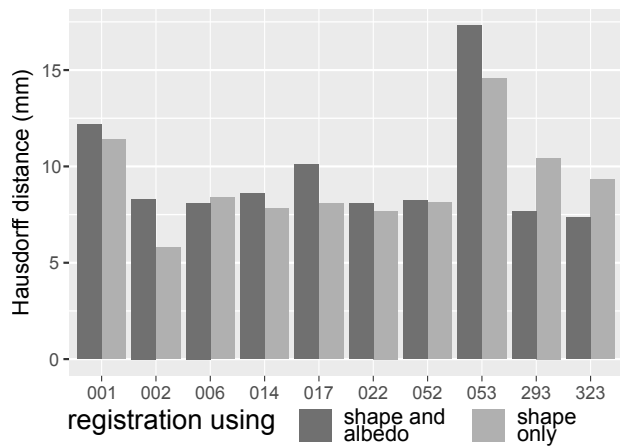


Figure 9: The Hausdorff distance between the landmarks of each of the registered meshes and the landmarks of the corresponding face scan.

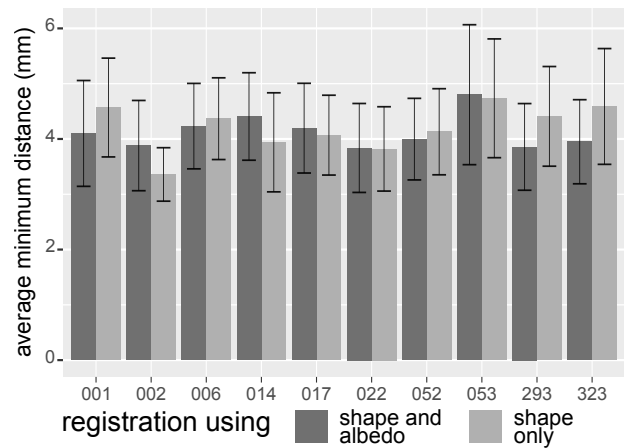


Figure 10: The average distance between each landmark in each of the registered meshes and the closest landmark in the corresponding face scan, with error bars ( $\pm 1.96$  standard error).

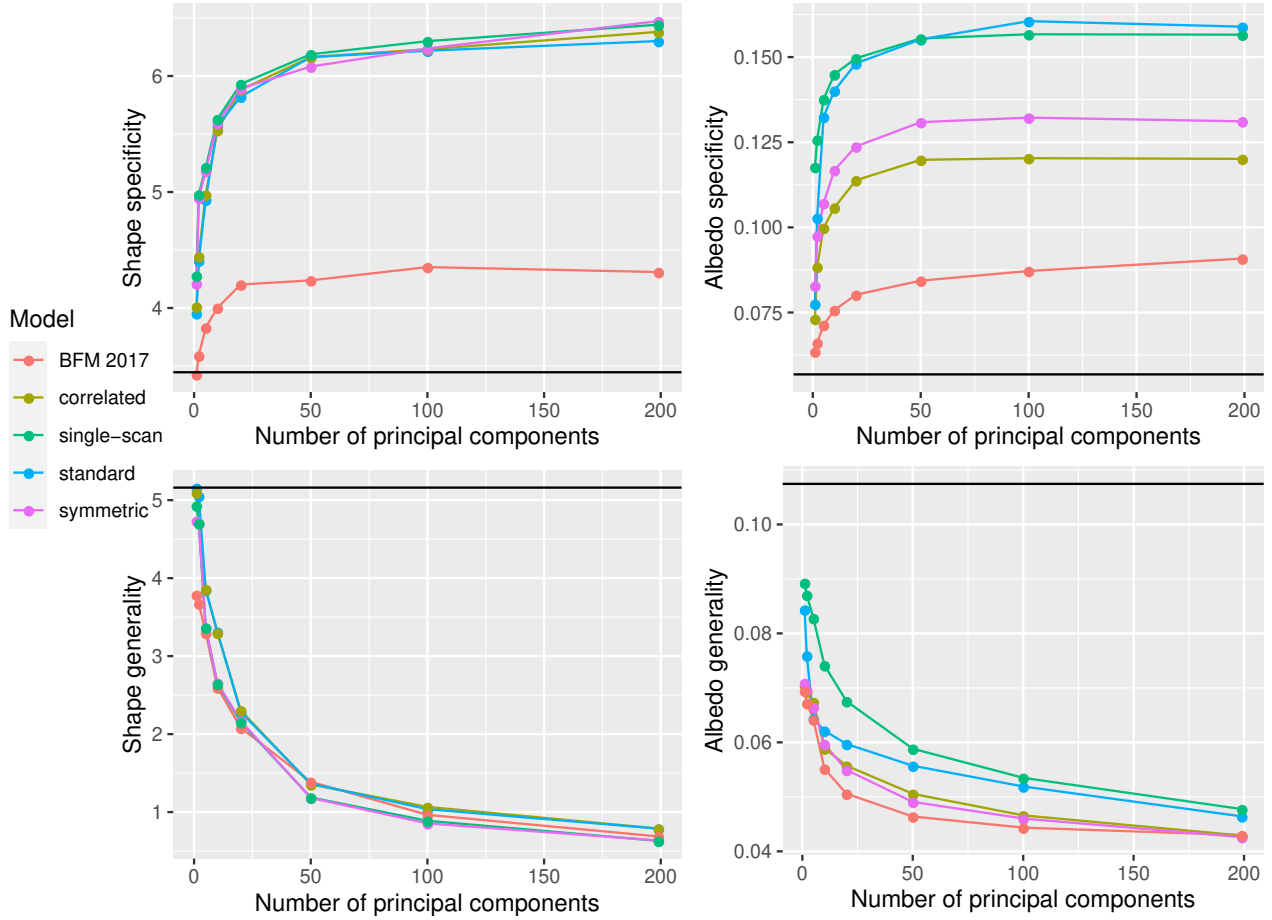


Figure 11: A plot of the specificity, generalization, and compactness [37] of our 3DMMs’ relative to the 2017 Basel Face Model [13]. “standard”, “correlated”, and “symmetric” refer to versions of the standard-full, correlated-full, and symmetric-full models built using the mean of the 2017 Basel Face Model, while the “single-scan” results are an average of the performance of the various symmetric- $x$  models. The scans included with the 2009 Basel Face Model [28] were used as a dataset; for the symmetric- $x$  3DMMs, the scan used to construct the 3DMM was excluded. See Section E for more details.



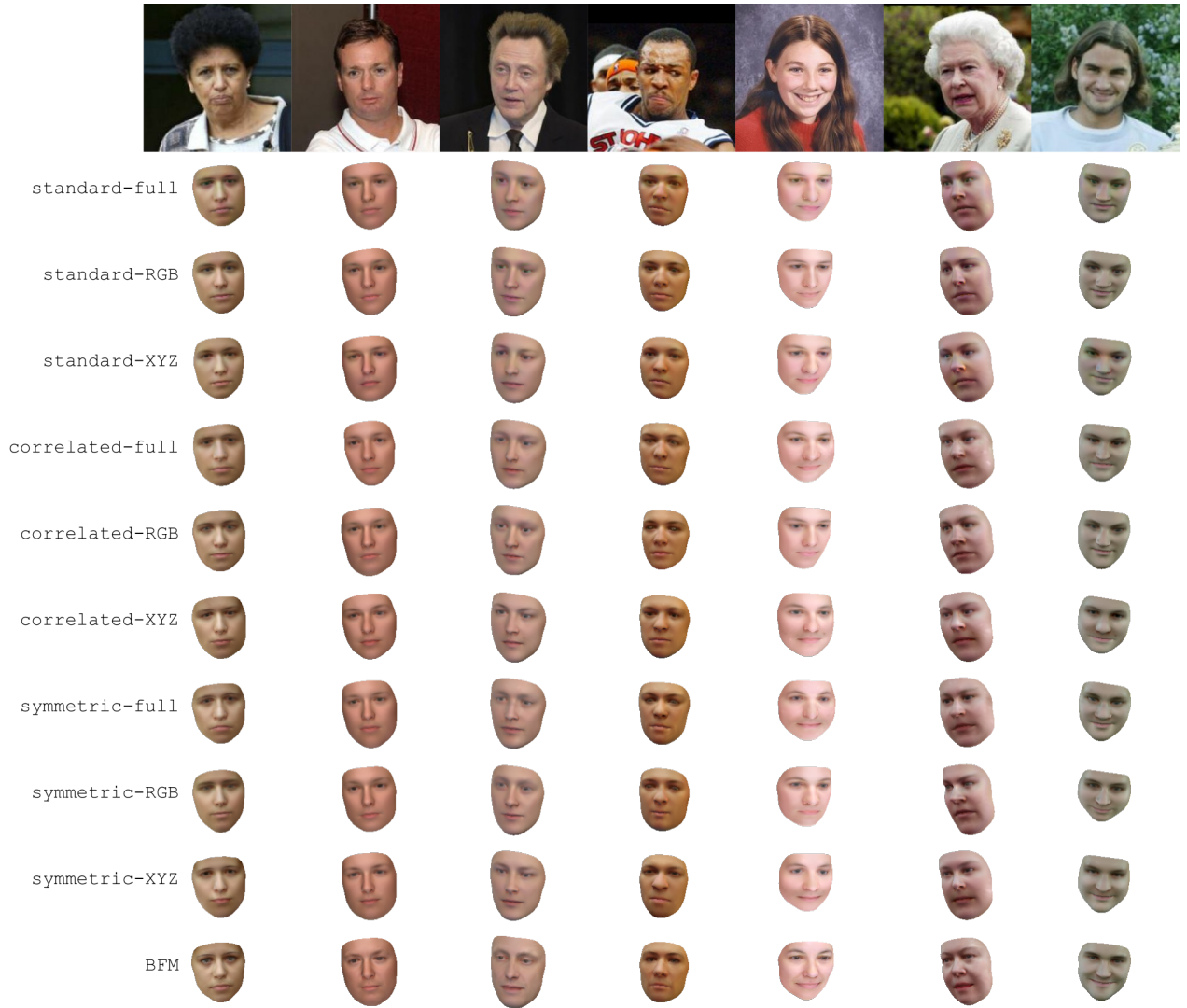


Figure 12: The face reconstructions produced from all the 3DMMs built using the mean of the 2019 Basel Face Model [13] on natural images from the Labeled Faces in the Wild dataset [16], as well as the reconstructions produced using the 2019 Basel Face Model itself (“BFM”).

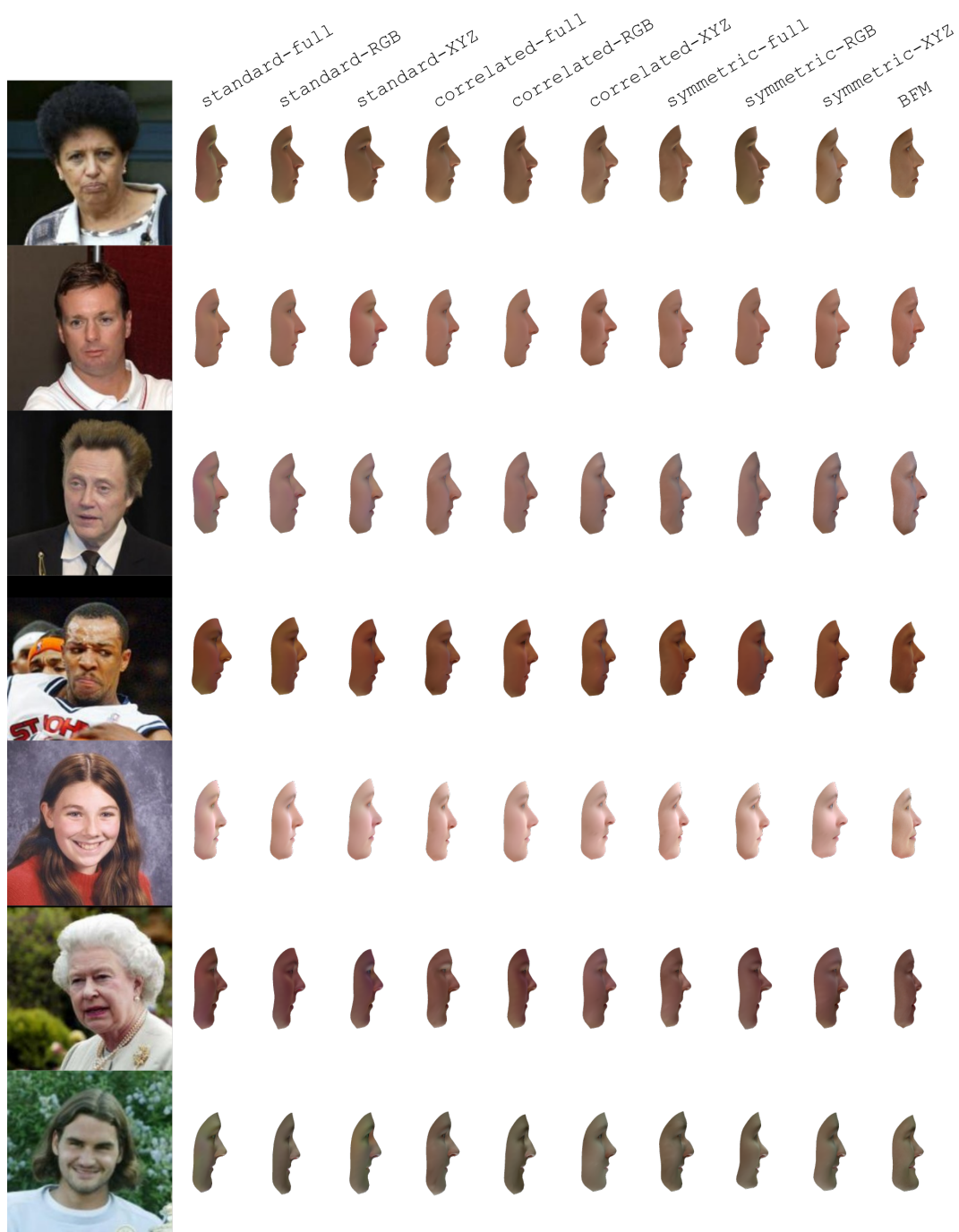


Figure 13: Side views of the reconstructions presented in Figure 12.



Figure 14: The face reconstructions produced from all 3DMMs built using the symmetric-full kernel and scans included with the 2009 Basel Face Model [28] on natural images from the Labeled Faces in the Wild dataset [16].

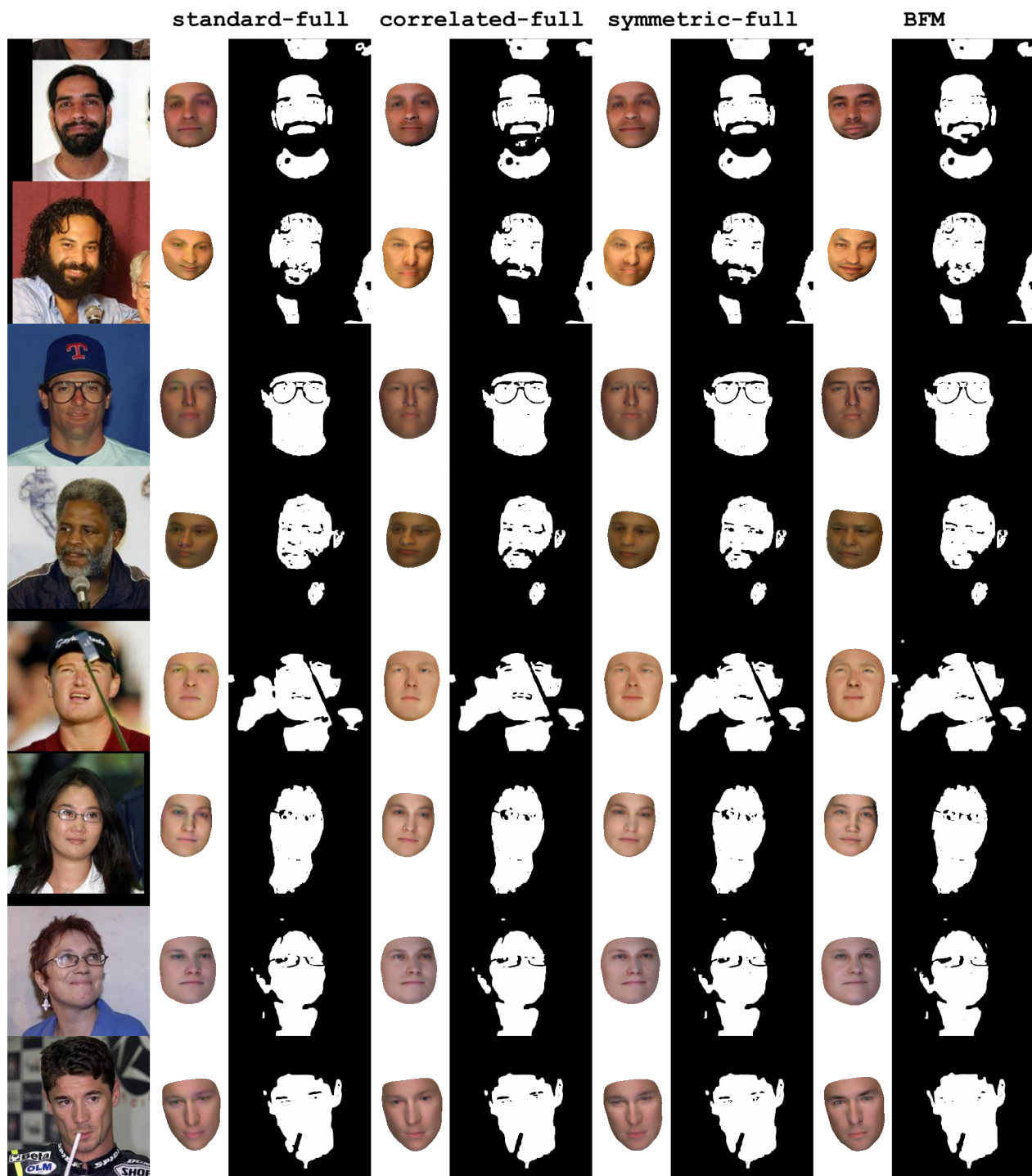


Figure 15: The face reconstructions produced by our standard-full, correlated-full, and symmetric-full models, as well as the 2019 Basel Face Model [13] (“BFM”), on images from the Labeled Faces in the Wild dataset [16], produced using the occlusion-aware MCMC method described in [11]. Both the segmentation masks and face reconstructions were inferred purely with top-down inference.